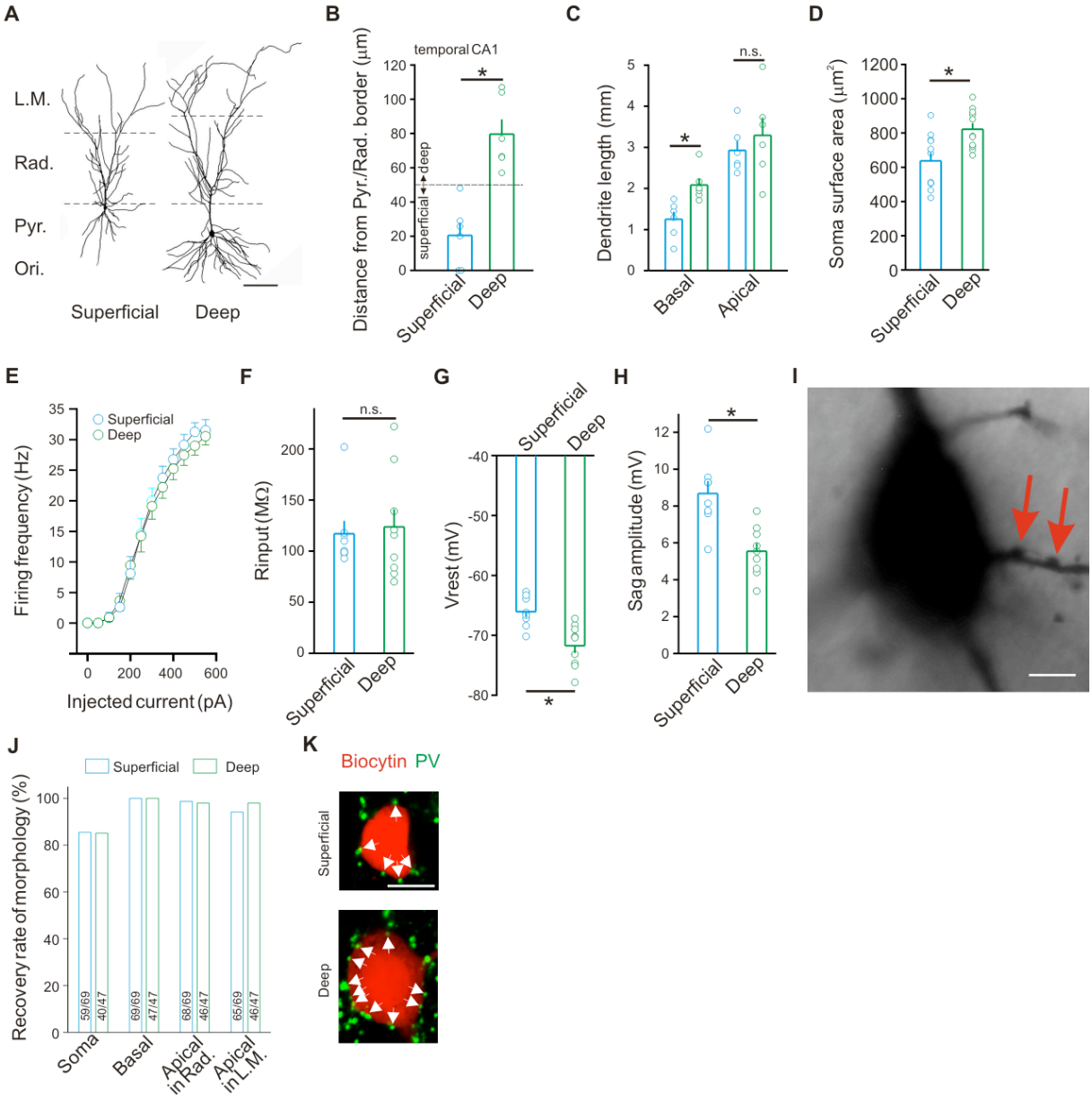

Supplementary Figure 1, related to Figure 1

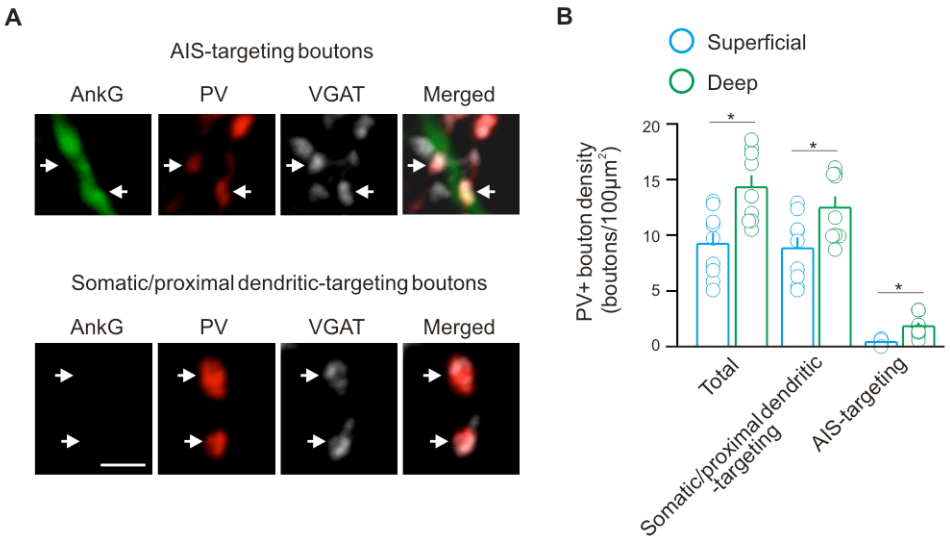

Supplementary Figure 2, related to Figure 2

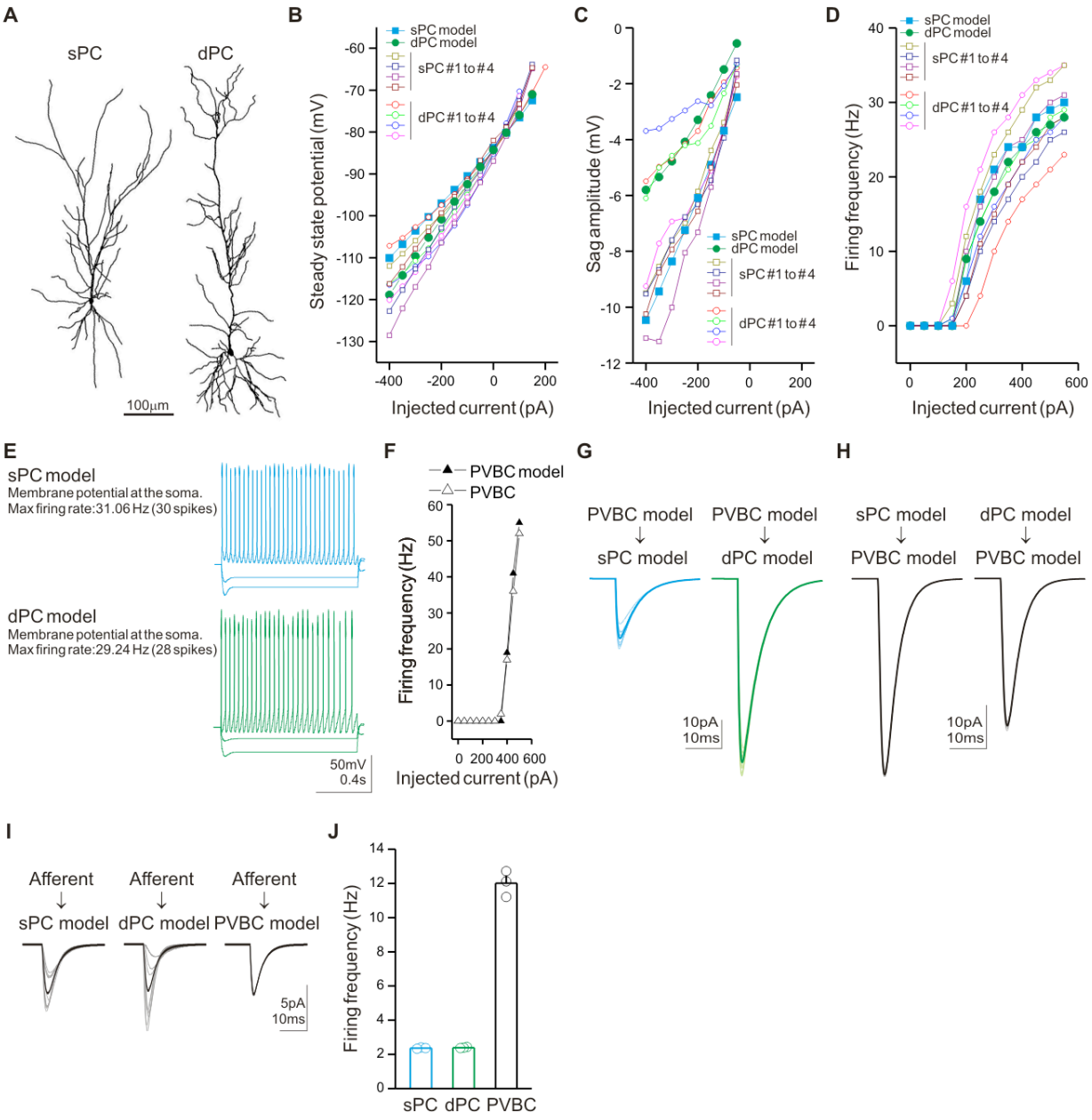

Supplementary Figure 3, related to Figure 4

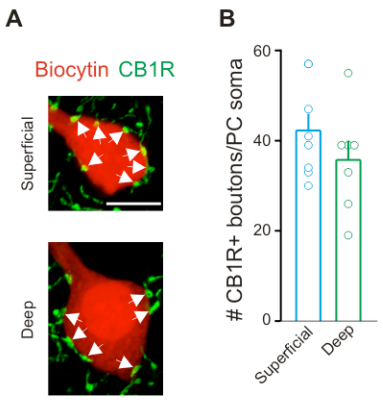

Supplementary Figure 4, related to Figure 5

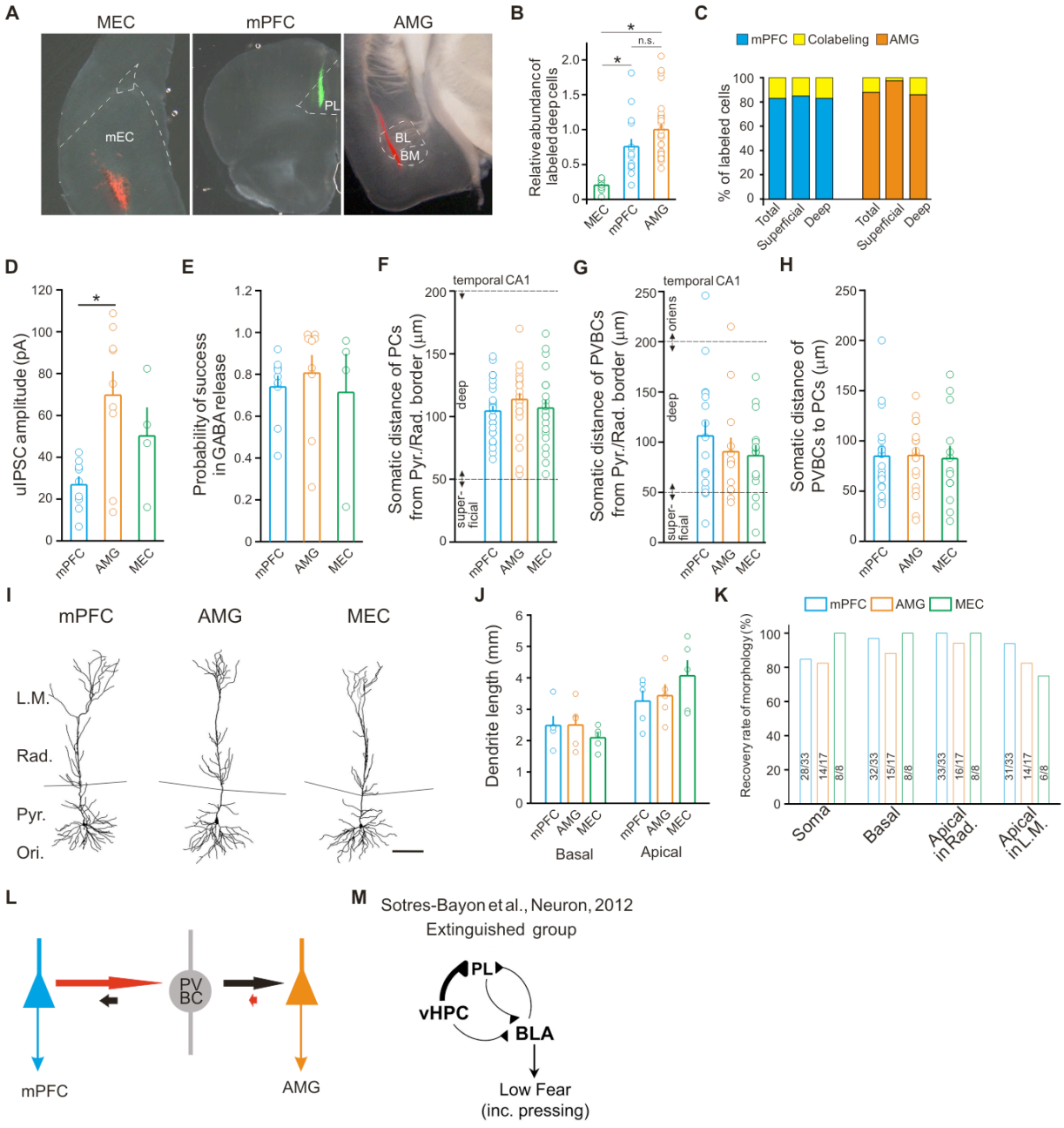

Supplementary Figure 5, related to Figure 6

Figure S1, related to Figure 1. Morphological and intrinsic electrophysiological properties of CA1 sPC and dPCs. (A) Representative camera lucida drawings of an sPC and a dPC; scale bar: 100μm. **(B)** Soma location (with respect to the Pyr/Rad border) of reconstructed sPCs (n=6) and dPCs (n=6) from the temporal hippocampus used for morphological analysis in panel C. **(C)** Dendritic length of the dPCs (n=6) and sPCs (n=6) based on Neurolucida reconstruction and analysis. **(D)** Soma surface area of dPCs (11 biocytin-filled dPCs) and sPCs (11 biocytin-filled sPCs) analyzed using Z-stacked confocal images and analyzed with the Volocity software (see Experimental Procedures). **(E to H)** I-F curves (two-way ANOVA, $p>0.4$), and input resistance, resting membrane potential and sag amplitude of sPCs and dPCs (sPC, n=8; dPC, n=9). **(I)** Light microscope image showing two putative synapses (red arrows) of a PVBC onto a proximal basal dendrite of a dPC from the data set in Figure 1J; scale bar: 5μm. **(J)** Recovery rates of the somato-dendritic morphology of the paired recorded postsynaptic PCs. The numbers in bar graphs represent the number of successfully recovered / recorded cells. **(K)** Representative images illustrating more perisomatic PV^+ boutons in close juxtaposition (white arrows) with the somata of dPCs compared to sPCs (PCs were filled with biocytin *in vitro*); such perisomatic boutons were used in the bouton counts for Figure 1L. Means and SEM; asterisks: $p<0.05$; n.s., not significant, in this and all subsequent supplementary figures.

Figure S2, related to Figure 2. Immunocytochemical analysis of the relative contribution of PVBC versus axo-axonic (chandelier) cell boutons to the *in vivo* 2-photon imaging data in Figure 2. (A) Using triple immunocytochemical staining of PV/ankyrinG/VGAT, PV^+ AIS-targeting boutons can be distinguished from the also PV^+ somatic/proximal dendritic-targeting boutons. AnkyrinG was used to visualize axon initial segments (AIS); the vesicular GABA transporter VGAT was used to visualize presynaptic GABAergic terminals. Top row: white arrows point to AIS-targeting boutons which are double positive for PV and VGAT and are juxtaposed to $ankyrinG^+$ profiles (these are derived from axo-axonic cells); bottom row: white arrows point to boutons double positive for PV and VGAT that are not juxtaposed to $ankyrinG^+$ profiles (these are from PVBCs). The images are merged projection images of 5 Z-planes, 0.25μm Z step; scale bar: 2μm. **(B)** Summary data of total PV^+ boutons, somatic/proximal dendritic-targeting PV^+ boutons, and AIS-targeting PV^+ boutons in the superficial and deep sublayers.

Figure S3, related to Figure 4. Biological data-derived computational network model used in the simulations in Figure 4C-F, including the morphology, intrinsic and synaptic properties of the PCs/PVBCs. (A) Pyramidal cell morphology used for the sPC (left) and dPC model (right). Somatic surface areas were set to 829 μm^2 (dPC, experimental cell surface area was 822 μm^2) and 640 μm^2 (sPC, experimental cell surface area was 636 μm^2). **(B)** Steady state potential of the model and biological cells in response to subthreshold current injections. Solid squares and circles represent sPC model and dPC model, respectively; open squares and circles represents biological sPCs and dPCs, respectively (B to D). **(C)** Sag amplitude of the model and biological cells in response to hyperpolarizing current injections. Note that sag amplitude is larger in sPCs compared to dPCs. **(D)** Firing frequency of model and biological cells in response to suprathreshold current injections. **(E)** Voltage traces of the sPC (top) and dPC model (bottom) in response to current steps (-400, -200, +550pA from -84.6 mV). **(F)** Firing frequency of model and biological PVBCs in response to suprathreshold current injections. (**G and H**) Paired recordings from 10 randomly chosen model cells of each type from the network; average responses shown in thick lines. (G) IPSCs recorded in sPC (left) and dPC (right) model in response to a single action potential from a presynaptic PVBC. (H) EPSCs recorded in a PVBC in response to a single action potential from an sPC (left) or dPC (right). (**I**) EPSCs recorded in an sPC (left), dPC (center), and PVBC (right) model neuron in response to afferent excitation. (**J**) Average firing rates of cells in the network model under control conditions.

Figure S4, related to Figure 5. Lack of difference in the number of $CB1R^+$ boutons around the somata of sPCs and dPCs. (A) Representative immunocytochemical images illustrating similar numbers of perisomatic $CB1R^+$ boutons in close juxtaposion (white arrows) with the somata of sPCs (top) compared to dPCs (bottom); such perisomatic boutons were used for the bouton counts shown in panel B. **(B)** Summary data of the number of $CB1R^+$ boutons around the soma of dPCs and sPCs.

Figure S5, related to Figure 6. Retrograde labeling of dPCs projecting to the mPFC, AMG and MEC and their synaptic connectivity with the PVBCs. (A) Representative images of fluorescent microsphere injection sites into MEC (left), mPFC (center), and AMG (right). PL, prelimbic; BL/BM, basolateral and basomedial AMG nuclei. **(B)** Relative abundance of labeled

PCs. Note that all data in this figure came from the temporal CA1. **(C)** Summary of single-labeled $_{mPFC}$PCs (blue, 271 PCs) and $_{AMG}$PCs (orange, 410 PCs), and double-labeled $_{mPFC+AMG}$PCs (yellow, 56 PCs) following injections of red and green retrograde tracers into the mPFC and AMG in 3 mice. (**D and E**) Summary of uIPSC amplitudes (including successful events only, not failures) and probability of success in GABA release from paired recordings between PVBCs and the long-distance projecting dPCs. **(F and G)** Summary of somatic location of the recorded dPCs and PVBCs with respect to the Pyr/Rad border. (**H**) Summary of somatic distances between the PVBCs and dPCs from the paired recordings. **(I)** Camera lucida drawings of an $_{mPFC}$dPC, an $_{AMG}$dPC, and an $_{MEC}$dPC. Scale bar: 100μm. **(J)** Dendritic length of the differentially projecting dPCs ($_{mPFC}$PC, n=5; $_{AMG}$PC, n=5; $_{MEC}$PC, n=5; p>0.5). **(K)** Recovery rates of somato-dendritic morphology of the PCs after paired recordings. The numbers in bar graphs represent the number of successfully recovered / recorded cells. (**L and M**) Schematic diagrams illustrating the potential relevance of our findings to the circuitry underlying fear extinction proposed by Sotres-Bayon et al., 2012; see Discussion for details. **(L)** Schematic representation of the biased, non-uniform interaction between $_{AMG}$dPCs and $_{mPFC}$dPCs via PVBCs (based on Figure 6G; length of red and black arrows is proportional to the experimentally observed mean euI/EPSC amplitudes times connection probability). (**M**) Schematic summary diagram adopted, with minor modifications, with permission from Sotres-Bayon et al., 2012. The authors concluded based on unit recordings in contextual fear conditioned animals that during the extinction phase, the output to the mPFC from the ventral hippocampus increases while the hippocampal output to AMG simultaneously decreases. Our results illustrated in (L) are consistent with the latter finding, suggesting that the increases in the hippocampal output to the mPFC may automatically decrease the hippocampal outflow to the fear centers in the AMG due to the particular, biased organization of the $_{mPFC}$dPC-PVBC-$_{AMG}$dPC microcircuit in the temporal (ventral) hippocampus.